

On the maximum conversion efficiency into the 13.5-nm extreme ultraviolet emission under a steady-state laser ablation of tin microspheres

M. M. Basko

Citation: *Physics of Plasmas* **23**, 083114 (2016); doi: 10.1063/1.4960684

View online: <http://dx.doi.org/10.1063/1.4960684>

View Table of Contents: <http://scitation.aip.org/content/aip/journal/pop/23/8?ver=pdfcov>

Published by the [AIP Publishing](#)

Articles you may be interested in

[Enhancing extreme ultraviolet photons emission in laser produced plasmas for advanced lithography](#)

Phys. Plasmas **19**, 083102 (2012); 10.1063/1.4742159

[Dynamics of laser-produced Sn microplasma for a high-brightness extreme ultraviolet light source](#)

Appl. Phys. Lett. **98**, 201501 (2011); 10.1063/1.3589359

[Theoretical investigation of the spectrum and conversion efficiency of short wavelength extreme-ultraviolet light sources based on terbium plasmas](#)

Appl. Phys. Lett. **97**, 231501 (2010); 10.1063/1.3524494

[Simplified one-dimensional calculation of 13.5 nm emission in a tin plasma including radiation transport](#)

J. Appl. Phys. **106**, 113303 (2009); 10.1063/1.3264692

[Angular emission and self-absorption studies of a tin laser produced plasma extreme ultraviolet source between 10 and 18 nm](#)

Appl. Phys. Lett. **92**, 231503 (2008); 10.1063/1.2945645

Ready, set, simulate.

REGISTER FOR THE COMSOL CONFERENCE >>



On the maximum conversion efficiency into the 13.5-nm extreme ultraviolet emission under a steady-state laser ablation of tin microspheres

M. M. Basko^{a)}

Keldysh Institute of Applied Mathematics, Moscow, Russia and RnD-ISAN/EUV Labs, Moscow, Troitsk, Russia

(Received 1 June 2016; accepted 27 July 2016; published online 15 August 2016)

Theoretical investigation has been performed on the conversion efficiency (CE) into the 13.5-nm extreme ultraviolet (EUV) radiation in a scheme where spherical microspheres of tin (Sn) are simultaneously irradiated by two laser pulses with substantially different wavelengths. The low-intensity short-wavelength pulse is used to control the rate of mass ablation and the size of the EUV source, while the high-intensity long-wavelength pulse provides efficient generation of the EUV light at $\lambda = 13.5$ nm. The problem of full optimization for maximizing the CE is formulated and solved numerically by performing two-dimensional radiation-hydrodynamics simulations with the RALEF-2D code under the conditions of steady-state laser illumination. It is shown that, within the implemented theoretical model, steady-state CE values approaching 9% are feasible; in a transient peak, the maximum instantaneous CE of 11.5% was calculated for the optimized laser-target configuration. The physical factors, bringing down the fully optimized steady-state CE to about one half of the absolute theoretical maximum of CE $\approx 20\%$ for the uniform static Sn plasma, are analyzed in detail. *Published by AIP Publishing.* [<http://dx.doi.org/10.1063/1.4960684>]

I. INTRODUCTION

The commercial success of the extreme ultraviolet (EUV) lithography depends crucially on the conversion efficiency (CE) into the 2% bandwidth around $\lambda = 13.5$ nm (the *in-band* emission) of the respective driver energy.^{1,2} The 2% bandwidth is determined by high reflectivity of the Mo/Si multilayer mirrors, used in the lithography optical schemes. For the laser-plasma EUV sources, CE is defined as the ratio of the in-band energy (power), emitted into 2π sr towards the primary mirror, to the total energy (power) of the driving laser pulse.

Previous theoretical attempts to calculate maximum possible CE have either been performed under highly idealized assumptions^{3–6} or relied on multidimensional radiation-hydrodynamics (RHD) simulations for only limited combinations of target and laser parameters.^{7,8} Here, we undertake a more general task of full optimization for the highest possible CE that could be attained by *steady-state* laser ablation of mass-limited tin (Sn) targets in the two-dimensional (2D) flow geometry. Setting up the problem as a steady-state one is, on the one hand, suggested by experimental observations,⁹ and, on the other hand, simplifies the complex parametric analysis of the general optimization problem, allowing, as is shown below, its reduction to optimization with respect to only two essential parameters; the latter can be already carried out with a reasonably adequate 2D RHD code.

Clearly, to have any bearing on reality, a steady-state ablation flow must (i) have a divergent pattern in order to let the main laser pulse enter—and the in-band emission exit—the EUV emission zone with the minimum attenuation en route and (ii) be essentially two-dimensional because the

driving laser beam comes from only one side. Hence, all the analysis in this work is performed for a steady ablation of small spherical droplets of tin, irradiated from one side by non-divergent (i.e., with zero numerical aperture) laser beams. To gain independent control of the two principal parameters, governing CE, namely, of the spatial scale and the temperature of the EUV emission zone, we consider a scheme where Sn droplets are simultaneously irradiated by two colinear different-color laser beams. The main energy, converted into EUV, is provided by a “master” laser pulse (in this work it is the CO₂ laser), which is absorbed in a plasma cloud preconditioned by a separate “slave” laser pulse. Because the principal mission of the “slave” pulse is to ensure efficient mass ablation at low energy cost, a preferable choice would be a short-wavelength laser. Here, we consider different harmonics ($1\omega - 4\omega$) of the Nd:YAG as possible candidates for the “slave” laser.

The idea to use two different-color lasers is not new, and has already been advocated theoretically^{7,8,10} and tested experimentally.^{11,12} Here, we use two lasers as a sort of two “handles,” turning which one can perform full optimization and find practically feasible absolute maxima for both the steady-state and the transient-peak CE values. In the process, the key physical effects, which keep practically feasible CE values significantly below the absolute theoretical maximum of $\approx 20\%$, are identified and analyzed. It is also established how the main characteristics of the ablation flow and of the in-band EUV source scale with the Sn-droplet size and the principal laser parameters.

We begin by demonstrating in Sec. II that the theoretical maximum of CE lies near 20%, and by revealing the general optimum conditions under which it occurs. Section III describes briefly the physical model implemented in the RALEF-2D code, used to solve the optimization problem. In

^{a)}Electronic mail: mmbasko@gmail.com. URL: <http://www.basko.net>

Sec. IV, the 2D ablation flow, created by the “slave” laser alone, is analyzed; approximate formulae for the dependence of its characteristics on the laser pulse parameters and the droplet radius are derived and verified by the 2D simulations. The optimization procedure for CE is formulated in Sec. V, with the results of optimization presented in Sec. VI. And finally, Sec. VII demonstrates what can be expected when the “slave” pulse is omitted.

II. OPTIMUM PLASMA PARAMETERS AND GENERAL GUIDELINES FOR LASER-TARGET OPTIMIZATION

To get a clear idea of what maximum CE values might be expected from the laser driven EUV sources, we start with the notion of the *spectral purity* (SP). We define the *instantaneous* SP for a given isolated plasma volume as the fraction of radiative power, emitted by this volume within the 2% bandwidth around 13.5 nm, relative to the total (i.e., spectrally integrated, or *broad-band*) radiative power escaping from this volume; all the radiation emitted into the full 4π -sr solid angle is accounted for.

In a static situation, the SP is fully determined by the spatial distribution of the plasma temperature T and density ρ , and can be calculated by solving the corresponding system of rate equations of the collisional-radiative (CR) plasma model^{13,14} coupled to the equation of spectral radiative transfer. In the limiting case of a black-body emitter, the maximum SP is attained at $T = 23.5$ eV and amounts to meagre 1.5%.^{4,5} Much higher SP values can be expected from translucent Sn plasmas, as is shown in Fig. 1.

The SP curves in Fig. 1 were calculated for three uniform Sn-plasma cylinders of different size, whose initial temperature and density were set equal to $T = 50$ eV and $\rho = 10^{-4}$ g/cc. The simulations were performed with the 2D RHD code RALEF (for more details, see Sec. III below). In each case, the plasma cylinder was allowed to cool down exclusively by losing energy via thermal radiation; the hydrodynamic expansion was artificially suppressed by zeroing the plasma pressure. As the temperature drops in time (remaining in all the three cases practically uniform over the

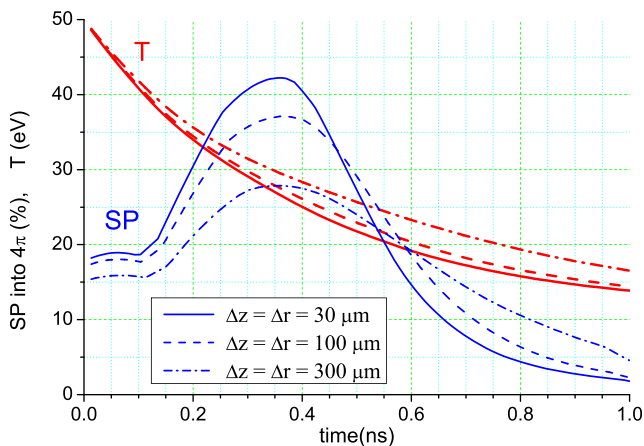


FIG. 1. Spectral purity of the thermal radiation, emitted by static uniform Sn-plasma cylinders at a fixed density $\rho = 10^{-4}$ g/cc in the process of their radiative cooling from the initial temperature of $T = 50$ eV as calculated by the RALEF code.

considered volume), the ratio of the in-band to the total radiative cooling power produces the SP(t) curve; by mapping the SP(t) curve to the $T(t)$ curve from the same simulation, we obtain the SP(T) dependence. Importantly, thus obtained SP(T) function does not depend on the decay rate of T because all the simulations have been done by using the spectral opacity tables, prepared under the quasi-stationary assumption¹⁵ for the level kinetics, i.e., by assuming that the populations of all the ionization stages and excited levels instantaneously relax to the steady-state solution of the corresponding rate equations for given ρ and T . It is important to emphasize that the curves in Fig. 1 have been obtained under exactly the same approximations in the CR plasma model as all the other calculations of CE for the laser ablated Sn droplets discussed in this work.

In all the three cases, shown in Fig. 1, a well defined maximum of SP(T) is observed within the temperature interval $25 \text{ eV} \lesssim T \lesssim 32 \text{ eV}$, where the mean ionization degree of tin is $z_i \approx 10 - 11$. The highest value of $SP \approx 40\%$ is reached in the optically thin limit of $\tau_{uv} \ll 1$, where τ_{uv} is the Planck mean optical thickness of the considered volume within the relevant 2% bandwidth. This high value, exceeding the black-body SP by about a factor 30, is produced by a high concentration around $\lambda = 13.5$ nm of numerous transitions in the $\text{Sn}^{8+} - \text{Sn}^{12+}$ ions,¹⁶ as is illustrated by the opacity plot in Fig. 2. Note that essentially the same absolute maximum of $SP \approx 40\%$ was reported earlier^{7,8} (though at a somewhat higher temperature of $T \approx 40 - 45$ eV) by an independent group from Japan.

By applying Eq. (20), given below, to the three cases of Fig. 1, one calculates $\tau_{uv} \approx 0.1, 0.3,$ and 1.0 in the z direction at $T = 30$ eV and $z_i = 10$. One sees that with the increasing τ_{uv} the peak SP(T) value monotonically decreases due to the self-absorption of the in-band radiation; in the limit of $\tau_{uv} \rightarrow \infty$, it should approach the black-body value of 1.5%.

The results shown in Fig. 1 imply that having prepared a static, uniform, and optically thin (with $\tau_{uv} < 0.3$) Sn-plasma volume at the optimum temperature of $T \approx 30$ eV, one could, in principle, reach a steady-state efficiency of CE $= \frac{1}{2} SP \approx 20\%$ (because for CE only 2π steradians count)

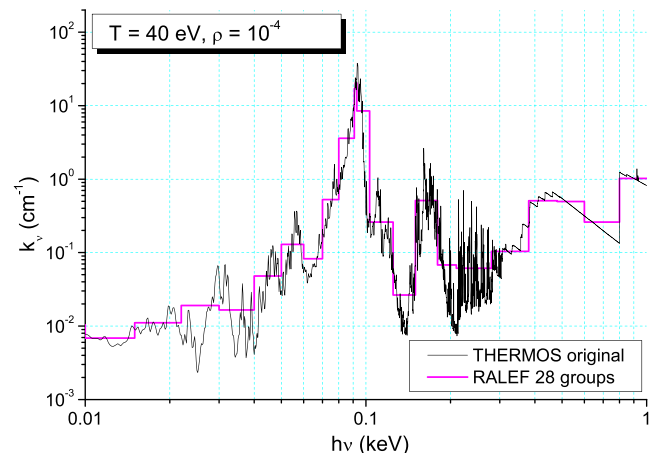


FIG. 2. Spectral absorption coefficient of tin at $\rho = 10^{-4}$ g/cc and $T = 40$ eV. Thin black curve: the original data from the THERMOS code. Thick red histogram-like curve: group-averaged values used in the RALEF simulations.

once the radiative losses are compensated by a steady external heating source. If the external heating is provided by a laser, the optimum plasma temperature (in combination with its density in the laser absorption zone) actually fixes the optimum laser irradiance I_{ml} ; in our model, the optimum irradiance by a CO₂ laser falls in the range $I_{ml} = (6 - 8) \times 10^9 \text{ W/cm}^2$.

The above considerations lead to the following general prescriptions for achieving the maximum possible CE:

- (i) The “master” laser pulse should be fully absorbed in the ablated plasma, i.e., the laser flux missing the target and reflected back must be minimized.
- (ii) The fraction of the absorbed laser energy, converted into the kinetic energy of the plasma flow, must be reduced to a minimum.
- (iii) All the laser light should be absorbed near the optimum temperature (where SP peaks) of the ablated Sn plasma.

Condition (i) implies that the distribution of the free electron density n_e must be nearly uniform—because negligible reflection and refraction of the CO₂ laser light are only possible when the spatial gradients of n_e are sufficiently weak. In combination with condition (iii), this means that the temperature distribution across the laser absorption zone must also be nearly uniform. In this study, by performing extensive 2D RHD simulations, we explore how closely one can approach such an ideal configuration in a realistic environment, and how far below 20% the optimized realistic CE values can turn out to be.

III. SIMULATION MODEL

All the 2D RHD simulations have been done with the RALEF-2D code,^{17,18} whose hydrodynamics module is based on the upgraded version of the CAVEAT package.¹⁹ The one-fluid one-temperature hydrodynamics equations are solved in two spatial dimensions [in either Cartesian (x, y) or axisymmetric (r, z) coordinates] on a multi-block structured quadrilateral grid by a second-order Godunov-type numerical method. An important ingredient is the mesh adaptivity, realized within the arbitrary Lagrangian-Eulerian approach.¹⁹

The numerical algorithms for thermal conduction and radiation transport have been developed within the unified symmetric semi-implicit scheme^{20,21} with respect to time discretization. Radiation energy transport is described by the quasi-static transfer equation,

$$\mathbf{\Omega} \cdot \nabla I_\nu = k_\nu (B_\nu - I_\nu), \quad (1)$$

for the spectral radiation intensity $I_\nu = I_\nu(t, \mathbf{x}, \mathbf{\Omega})$; here, $\mathbf{\Omega}$ is the unit vector in the direction of photon propagation, $B_\nu(T)$ is the spectral intensity of the equilibrium black-body radiation; the term $c^{-1} \partial I_\nu / \partial t$ (where c is the speed of light) is neglected. Coupling to the fluid is represented by the volume-specific radiative heating rate,

$$Q_r = -\text{div} \int_0^\infty d\nu \int_{4\pi} I_\nu \mathbf{\Omega} d\mathbf{\Omega}. \quad (2)$$

In the RALEF code, the classical S_n method is used to treat the angular dependence of the radiation intensity $I_\nu(t, \mathbf{x}, \mathbf{\Omega})$, and the method of short characteristics²² to integrate Eq. (1). The latter has an important advantage that every grid cell automatically receives the same number of light rays. Correct transition to the diffusion limit²³ on non-orthogonal grids is achieved by special combination of the first- and second-order interpolation schemes in the finite-difference approximations to Eqs. (1) and (2).

The equation of state of tin has been constructed by using the FEOS model,²⁴ which allows adequate description of high-temperature plasma states together with the low-temperature liquid-gas phase coexistence region. The model for thermal conductivity is based on a semi-empirical expression for the transport cross-section of the electron-ion collisions,²⁵ which allows a smooth matching of the Spitzer plasma conductivity to that of metals near normal conditions.

Calculation of the adequate spectral absorption coefficient k_ν for the transfer equation (1) is a separate complex problem. Here, we use the approach¹⁵ based on quasi-stationary opacity tables that are prepared beforehand by finding a steady-state solution (for any given ρ, T pair) to a large system of CR rate equations for populations of the relevant atomic levels. The key uncertainty in this procedure is the a priori unknown intensity I_ν of the local radiation field, which strongly affects the EUV emissivity of the Sn plasma.¹⁵ In this work, we used *partially opaque* k_ν tables, calculated with the THERMOS package¹³ under the assumption of a black-body radiation field within the 10% bandwidth around $\lambda = 13.5 \text{ nm}$, and zero radiation field outside this range. Such an approximation appears reasonable for the purposes of the present study, where the sought-for optimum plasma configurations have the optical thickness of the order of unity in the narrow bandwidth around 13.5 nm where k_ν peaks (see Fig. 2), and are optically thin for the rest of the spectrum. In all the RHD simulations, discussed below, 28 discrete spectral groups of variable width were used (as shown in Fig. 2), with two groups belonging to the 2% in-band interval.

The laser deposition was treated within a simplified model, where every elementary laser ray could propagate either forward or backward along a fixed straight trajectory; the absorption and reflection of laser light was calculated by solving the one-dimensional (1D) Helmholtz wave equation²⁶ along the propagation direction with an appropriate complex dielectric permittivity of the ablated plasma.²⁷ Laser refraction was deliberately ignored to avoid complications by the analysis of the CE-governing physics, which arise from the instability caused by the self-focusing (defocusing) of the laser beam [and the ensuing partially stochastic behavior of the instantaneous CE(t)] by its interaction with the 2D plasma flow. In all cases, a box-like focal spot profile was used.

IV. QUASI-STEADY-STATE DENSITY PROFILES PRODUCED BY THE “SLAVE” LASER

In this section, we analyze the spatial density distribution in the ablated plasma, created by the “slave” laser alone under the conditions of steady-state irradiation of an Sn

microsphere. The principal task of the “slave” pulse is to provide an abundant mass outflow at a minimum energy cost. Because of a much steeper dependence of the mass ablation rate j [$\text{g cm}^{-2} \text{s}^{-1}$] on the laser frequency ω_{sl} than on its intensity I_{sl} , it is advantageous to employ a short-wavelength laser—like one of the higher harmonics of Nd:YAG—at a relatively low irradiation intensity. As a reference case, the third harmonic of the Nd:YAG laser with

$$\lambda_{sl} = 352 \text{ nm}, \quad I_{sl} = 1.5 \times 10^9 \text{ W/cm}^2 \quad (3)$$

was chosen.

The scaling of j with $\omega_{sl} = 2\pi c/\lambda_{sl}$ and I_{sl} ,

$$j \propto \omega_{sl}^{2\nu_j} I_{sl}^{\delta_j}, \quad (4)$$

depends essentially on whether the laser flux is mainly absorbed at the critical surface or in the underdense corona,²⁸ and on the equation of state of the ablated material.²⁹ For tin, depending on the location of the absorption region (cf. cases I-Sn and II-Sn in Ref. 29)

$$2\nu_j \approx 1.7 \div 0.7, \quad \delta_j \approx 0.1 \div 0.3. \quad (5)$$

All the cases, simulated in the present study with I_{sl} varying in the range of $(0.5 - 5) \times 10^9 \text{ W/cm}^2$ and $266 \text{ nm} \leq \lambda_{sl} \leq 1 \mu\text{m}$, fall closer to the case II-Sn of absorption in the underdense corona and fit into a more narrow interval

$$2\nu_j \approx 1.0 \div 0.8, \quad \delta_j \approx 0.2 \div 0.3. \quad (6)$$

In this situation, however, the mass flux j depends also on the length scale of the density variation, which, for a short-wavelength “slave” laser, practically coincides with the droplet radius R_d ; hence, the term $\omega_{sl}^{2\nu_j}$ in Eq. (4) should actually be replaced by the combination $(\omega_{sl}^2/R_d)^{\nu_j}$ (see Ref. 29 for details).

As is clearly illustrated in Fig. 3, after the plasma flow relaxes to a steady-state regime (some 20–40 ns after the turn-on of the “slave” pulse), the flow pattern approaches a nearly spherically symmetric configuration—despite the fact that the droplet is irradiated from only one side. Because in a steady spherical flow the product $\rho u r^2$ is conserved, the asymptotic radial density profile can be approximated (see Fig. 4) to a reasonable accuracy as

$$\rho(r) = \rho_d \left(\frac{R_d}{r} \right)^2, \quad (7)$$

where the density,

$$\rho_d = \frac{j}{u}, \quad (8)$$

and the flow velocity u are considered to be independent of r , and R_d is the initial droplet radius. It should be emphasized that such an approximation applies exclusively to the supersonic laser corona above the critical surface of the “slave” laser, where u is only a weak function of r ; for this reason, and despite the fact that typically both the critical and the sonic surfaces lie close to the liquid droplet surface, the

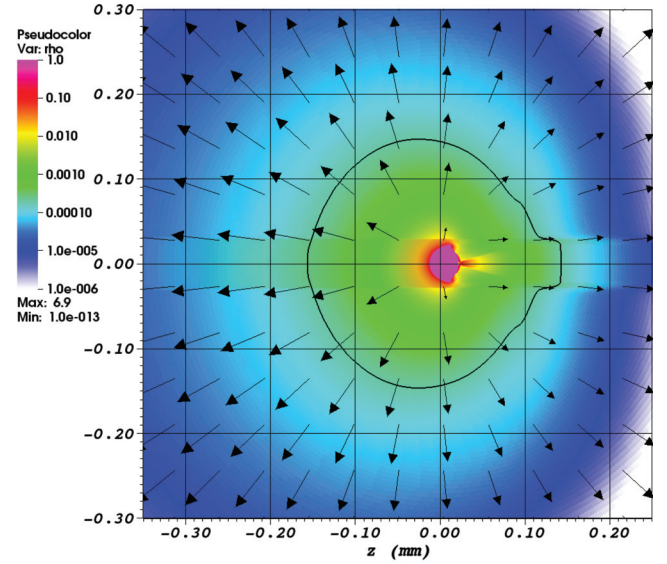


FIG. 3. 2D plasma density (in g/cc) map and velocity pattern around a 40- μm diameter droplet of tin, irradiated from left by a “slave” Nd:YAG- 3ω laser pulse with a constant intensity $I_{sl} = 1.5 \times 10^9 \text{ W/cm}^2$, at $t = 40 \text{ ns}$. The black contour corresponds to $\rho = 2 \times 10^{-4} \text{ g/cc}$ and marks approximately the position of the critical surface for the “master” CO_2 laser if it were turned on at that moment. Arrows indicate the magnitude and direction of the flow velocity. The local laser intensity is shown as a dark shadow.

reference density ρ_d must not be interpreted as the density of liquid tin.

If we assume for a moment that the droplet radius R_d is fixed, then the density ρ_d in Eq. (7) becomes a function of only two principal “slave” laser parameters λ_{sl} and I_{sl} ,

$$\rho_d = \rho_0 \lambda_{sl,\mu\text{m}}^{-2\nu_\rho} I_{sl,9}^{\delta_\rho}, \quad (9)$$

where $\lambda_{sl,\mu\text{m}}$ is the “slave” laser wavelength in micrometers, and $I_{sl,9}$ its intensity in 10^9 W/cm^2 . Note that the real density profiles are somewhat steeper than $\propto r^{-2}$ (as illustrated in Figs. 4 and 5) partially because the steady state has not been quite reached, and partially because the flow velocity u slightly grows with r .

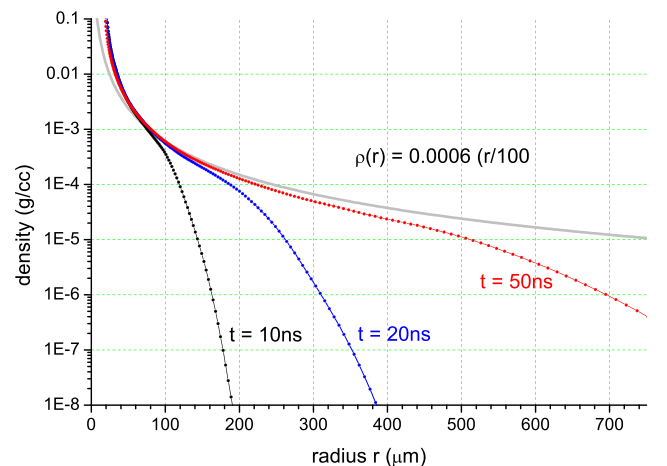


FIG. 4. Radial density profiles at different times in the direction towards the incoming “slave” laser beam for the reference case shown in Fig. 3.

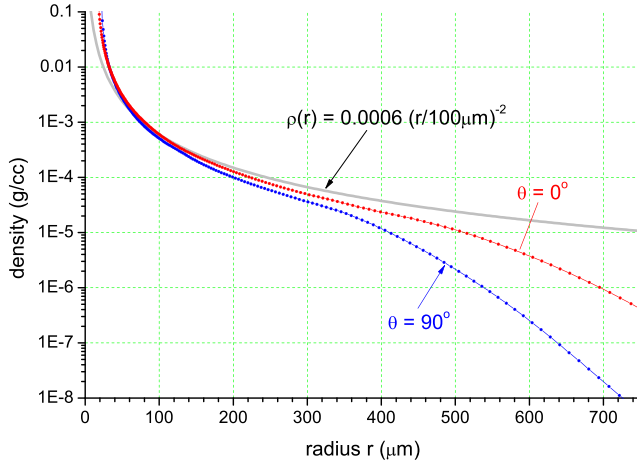


FIG. 5. Density profiles at $t = 50$ ns along two different radii for the reference case shown in Fig. 3.

The scaling exponents in Eq. (9) can be derived from the principal scaling exponents, introduced in Ref. 29, by noting that the density ρ scales as the ratio j^2/p_a , where p_a is the ablation pressure. Between the cases I-Sn and II-Sn in Ref. 29, the exponents in Eq. (9) span the range $2\nu_\rho \approx 2.5 \div 1.0$, $\delta_\rho \approx -0.32 \div -0.06$. For $R_d = 20 \mu\text{m}$ and the relevant ranges of λ_{sl} and I_{sl} , we find

$$\rho_0 \approx 3.2 \times 10^{-3} \text{ g/cc}, \quad 2\nu_\rho \approx 1.5, \quad \delta_\rho \approx -0.16. \quad (10)$$

Again, because we are closer to the case II-Sn than to I-Sn, the square of the wavelength λ_{sl}^2 in Eq. (9) should actually be replaced by the product $R_d \lambda_{sl}^2$.

As is indicated by the 2D color density map in Fig. 3 and confirmed by the lineout plots in Fig. 5, the dependence of the asymptotic radial profile (9) on the polar angle with respect to the laser axis is rather weak (at least over the laser-illuminated hemisphere) and, to a first approximation, can be neglected. Therefore, the radial dependence (7) can also be used to evaluate the effective transverse EUV source size, i.e., the radius of the EUV emitting plasma volume, defined here as the radius $r = R_{mc}$ of the critical surface for the “master” pulse where

$$n_e(R_{mc}) \equiv \frac{\rho_d z_i}{A m_u} \frac{R_d^2}{R_{mc}^2} = n_{ml,c} \equiv \frac{m_e \omega_{ml}^2}{4\pi e^2}. \quad (11)$$

Here, m_e and $-e$ are, respectively, the electron mass and its electric charge, m_u is the atomic mass unit, and $A = 118.7$ is the atomic mass of the target material (Sn). From Eqs. (9)–(11), taking into account the remark below Eq. (10) and setting $z_i = 10$, we calculate

$$R_{mc,\mu\text{m}} \approx 1.1 R_{d,\mu\text{m}}^{0.63} \lambda_{ml,\mu\text{m}} \lambda_{sl,\mu\text{m}}^{-0.75} I_{sl,9}^{-0.08}, \quad (12)$$

where $R_{mc,\mu\text{m}}$, $R_{d,\mu\text{m}}$, $\lambda_{ml,\mu\text{m}}$, and $\lambda_{sl,\mu\text{m}}$ are all measured in micrometers. The value of R_{mc} provides a good estimate for the optimal focal radius of the “master” pulse. Note that, for a fixed wavelength λ_{ml} of the “master” laser, the transverse size R_{mc} of the EUV source is almost exclusively controlled by the ratio R_d/λ_{sl} of the droplet radius to the “slave” laser wavelength.

V. THE OPTIMIZATION ALGORITHM

Since efficient EUV generation to a large extent depends on efficient laser absorption, we begin by evaluating the optical thickness τ_{ml} for the “master” laser along a power-law radial profile,

$$n_e(r) = n_{ml,c} \left(\frac{R_{mc}}{r} \right)^n, \quad (13)$$

of the free electron density n_e with respect to the inverse bremsstrahlung absorption; here, $n_{ml,c}$ is the critical density, defined in Eq. (11), and $n \geq 2$. Because we are interested in the optical thickness of the region where most of the laser energy is absorbed and most of the in-band EUV is expected to be generated (a “working” zone), we assume that this zone spreads over an interval

$$a_{uv} R_{mc} \leq r < +\infty, \quad (14)$$

where $a_{uv} \geq 1$ is an a priori unknown dimensionless coefficient, allowing for a possibility of the “master” pulse being fully absorbed well above the critical surface. Then

$$\tau_{ml} = \int_{a_{uv} R_{mc}}^{+\infty} k_{ml} dr, \quad (15)$$

where

$$\begin{aligned} k_{ml} &= \frac{16\pi\sqrt{2\pi}}{3} \frac{e^6 n_e^2 z_i}{c(m_e T)^{3/2} \omega_{ml}^2} \ln \Lambda_{ml} \\ &= 108 \frac{z_i \ln \Lambda_{ml}}{T_{heV}^{3/2} \lambda_{ml,\mu\text{m}}^2} \left(\frac{n_e}{n_{ml,c}} \right)^2 \text{ cm}^{-1} \end{aligned} \quad (16)$$

is the Kramers formula for the inverse-bremsstrahlung absorption coefficient³⁰ in the limit of $\hbar\omega_{ml} \ll T$. The Coulomb logarithm

$$\ln \Lambda_{ml} = \ln \left(\frac{4T}{\gamma_E \hbar\omega_{ml}} \right) \quad (17)$$

is obtained from the Gaunt factor in the Born approximation. In the above formulae, T_{heV} is the electron temperature in 100 eV, and $\ln \gamma_E = 0.577\dots$ is Euler’s constant. For the optimal temperature $T \approx 30$ eV and $\lambda_{ml} = 10.6 \mu\text{m}$, we calculate $\ln \Lambda_{ml} = 6.4$.

Having substituted Eqs. (13) and (16) into Eq. (15) and assuming an isothermal working zone, we find

$$\tau_{ml} = \frac{0.0108}{(2n-1) a_{uv}^{2n-1} T_{heV}^{3/2} \lambda_{ml,\mu\text{m}}} \left(\frac{R_{mc}}{\lambda_{ml}} \right). \quad (18)$$

As was established in many previous works,^{7,27–29} the approximation of an isothermal coronal flow is quite close to reality; otherwise, if departures from the temperature uniformity become significant, the temperature T in Eqs. (18), (19), and (21) should be understood as a certain average value across the working zone. The coefficient $a_{uv} \geq 1$ is found by applying the following argument. If τ_{ml} , calculated from Eq. (18) with $a_{uv} = 1$, turns out to be less than 1, then $a_{uv} = 1$; in this case

the “master” laser deposits its energy in the immediate vicinity of the critical surface; in the limit of $\tau_{ml} \ll 1$, a significant fraction of the incident laser energy may be reflected back and wasted for the EUV generation. If, however, Eq. (18) with $a_{uv} = 1$ yields $\tau_{ml} > 1$, then the value of $a_{uv} > 1$ is obtained from Eq. (18) by assuming $\tau_{ml} = 1$. Physically, this corresponds to a situation where the density gradient is so shallow that most of the incident laser light is absorbed and converted into EUV well before the critical surface in a plasma with $n_e \ll n_{ml,c}$.

The effective optical thickness τ_{uv} of the EUV emitting region for the in-band photons is evaluated in a similar fashion,

$$\tau_{uv} = \int_{a_{uv}R_{mc}}^{+\infty} k_{uv} dr \approx \frac{0.78}{(n-1)a_{uv}^{n-1}\lambda_{ml,\mu m}} \left(\frac{R_{mc}}{\lambda_{ml}}\right) \left(\frac{30 \text{ eV}}{T}\right)^{3.5}, \quad (19)$$

by making use of the Planck mean absorption coefficient,

$$k_{uv} \approx 70 \left(\frac{n_e}{10^{19} \text{ cm}^{-3}}\right) \left(\frac{30 \text{ eV}}{T}\right)^{3.5} \text{ cm}^{-1}, \quad (20)$$

for the in-band spectral range in the Sn plasma near optimal conditions; according to the THERMOS model for Sn, the above power-law approximation to $k_{uv}(n_e, T)$ applies at $10^{18} \text{ cm}^{-3} \lesssim n_e \lesssim 10^{20} \text{ cm}^{-3}$, $25 \text{ eV} \lesssim T \lesssim 40 \text{ eV}$; it is also consistent with the calculations of radiative properties of Sn ions in Ref. 31. Finally, from Eqs. (18) and (19), we calculate the ratio

$$\frac{\tau_{uv}}{\tau_{ml}} \approx 12 \frac{2n-1}{n-1} \frac{a_{uv}^n}{z_i \ln \Lambda_{ml}} \left(\frac{30 \text{ eV}}{T}\right)^2. \quad (21)$$

Now we recall that the highest possible CE values require $\tau_{ml} \simeq 1$ and $\tau_{uv} \ll 1$, i.e., the ratio τ_{uv}/τ_{ml} should be made as small as possible. On this premise, Eq. (21) implies that the optimum configurations would correspond to the lowest possible value of parameter $a_{uv} = 1$, i.e., to situations where the “master” pulse is mainly absorbed near the critical surface and the working zone lies immediately above it. Plasma configurations with $a_{uv} > 1$, where the “master” pulse encounters such a shallow density gradient that it is fully absorbed in the far underdense corona are inefficient because of the inevitable strong reabsorption of the in-band EUV photons in the working zone. Remarkably, this conclusion is virtually independent of the wavelength of the “master” laser λ_{ml} (once the weak dependence of $\ln \Lambda_{ml}$ on λ_{ml} is neglected) and of the steepness of the radial density profile represented by index n (variation of n from $n=2$ to $n=\infty$ changes the ratio τ_{uv}/τ_{ml} by only a factor 1.5, whereas $n < 2$ is not possible for our statement of the problem). So long as the optimal temperature T stays close to 30 eV, the ratio τ_{uv}/τ_{ml} is confined to a limited range of $\tau_{uv}/\tau_{ml} \approx 0.3 - 0.6$.

The above considerations lead to the following general logic of the optimization procedure for attaining maximum CE. Once the wavelength λ_{ml} of the “master” laser is fixed,

the asymptotic density profile (13) is characterized by a single parameter R_{mc} (hereafter we assume $n=2$). For any fixed value of R_{mc} , one carries out optimization with respect to the “master” irradiation intensity I_{ml} to determine the optimal plasma temperature T and its ionization degree z_i . Then, by varying R_{mc} , one establishes the absolute maximum of CE.

The fact that CE must have a maximum as a function of R_{mc} becomes evident after one assumes that, for different R_{mc} , the optimal values of T and z_i undergo little variation. Indeed, because τ_{uv} and τ_{ml} are both proportional to R_{mc} , while their ratio remains practically constant and not much different from $\simeq 0.5$, too low values of R_{mc} imply low efficiency of EUV generation because $\tau_{ml} \ll 1$ and the laser energy is poorly absorbed; in the opposite limit, too high values of R_{mc} lead to $\tau_{uv} > 1$ and quenching of the in-band emission due to its self-absorption.

Equation (12) tells us that, for a fixed value of λ_{ml} , variation of the source size R_{mc} can be achieved by changing either the droplet radius R_d , or the wavelength λ_{sl} of the “slave” laser, or both; variation of the intensity I_{sl} of the “slave” laser to this end makes little sense because of the weak dependence of R_{mc} on this parameter.

The inverse temperature dependence in Eq. (21) suggests that the effects of departure from the local thermodynamic equilibrium (LTE) and/or from the steady-state ionization equilibrium (due to a rapid transit of plasma elements through the working zone), which typically require higher T values to attain the same ionization states z_i , should lead to somewhat higher optimized CE values than those obtained in the LTE (or quasi-stationary non-LTE) approximation because the spectral purity of the EUV emission is in the first place determined by the presence of a specific group of Sn ions with $z_i = 8-12$.

VI. OPTIMIZED PERFORMANCE UNDER STEADY IRRADIATION BY TWO LASERS

A. Performance analysis for a representative case

Since adequate interpretation of the optimization results requires insight into the dynamical behavior of the irradiated target, we begin by analyzing the performance of a particular representative case, marked as case 61–13 in Fig. 10. Because it takes a few tens of nanoseconds for the “slave” laser to establish a sufficiently shallow density profile, it is advantageous to turn on the “master” pulse with a certain delay, i.e., at $t = t_{del} > 0$; in case 61–13, it was $t_{del} = 35 \text{ ns}$. We call the time interval $0 < t < t_{del}$ the *passive phase* of the operation cycle. Note that t_{del} is not treated as yet another optimization parameter because its value can be inferred from the radial density profiles (like in Fig. 4), obtained from a single run for the “slave” laser, as the time after which the density gradient in the vicinity of the “master” critical density ($\rho \simeq 2 \times 10^{-4} \text{ g/cc}$ for the CO₂ laser) stabilizes; for still longer t_{del} values, the CE ceases to depend on t_{del} whenever the “slave” power is small compared to the “master” one. As a practical rule, one may assume that the smallest acceptable values of t_{del} vary roughly in direct proportion to R_{mc} (see Table I).

TABLE I. Results of the 2D optimization with respect to the “master” laser intensity I_{ml} and the source size R_{mc} .

| | 10 μm | 20 μm | 30 μm | 50 μm |
|----------------|-------------------|-------------------|-------------------|-------------------|
| R_d | 10 μm | 20 μm | 30 μm | 50 μm |
| λ_{sl} | 352 nm | 352 nm | 352 nm | 266 nm |
| t_{del} | 35 ns | 35 ns | 40 ns | 60 ns |
| R_{mc} | 100 μm | 155 μm | 205 μm | 305 μm |
| $r_{foc,ml}$ | 90 μm | 130 μm | 170 μm | 280 μm |
| CE_{tp} | 11.1% | 11.5% | 11.3% | 11.0% |
| CE_{st} | 7.7% | 8.3% | 8.8% | 9.0% |
| CE | 8.0% | 8.4% | 8.7% | 9.0% |
| $f_{a,ml}$ | 82% | 85% | 89% | 97% |

Figure 6 displays temporal variation of different power components of the “master” pulse for the selected case 61–13, as well as that of the instantaneous conversion efficiency $CE(t)$. Note that CE is always defined with respect to the combined power (energy) of the two lasers. Once the main pulse is turned on, the instantaneous $CE(t)$ rapidly (within some 2 ns) rises to its peak value $CE_{tp} = 11.5\%$ at $t \approx 37.2$ ns, then drops and gradually approaches a steady-state value of $CE_{st} \approx 8.1\%$. The duration $\Delta t \approx 2$ ns is needed to heat up the plasma to its optimal working temperature of $T \approx 30$ eV. One also sees that at $t = 37$ – 38 ns, when $CE(t)$ peaks, the laser absorption is virtually 100%. That is, from the point of view of the laser absorption, the density profile, produced by the “slave” laser, could not be better. But then the question arises why the peak value CE_{tp} is still significantly below the theoretical maximum of $\approx 20\%$?

As already mentioned, even at 100% laser absorption, there still remain three important physical factors, degrading the CE, namely, (i) partial conversion of the laser energy into the plasma kinetic energy (plus, into its internal energy that is re-emitted elsewhere under non-optimal conditions); (ii) non-uniformity of the plasma state across the working zone (which manifests itself in that one part of the laser absorbing volume is underheated and the other overheated with respect to the optimum temperature); and (iii)

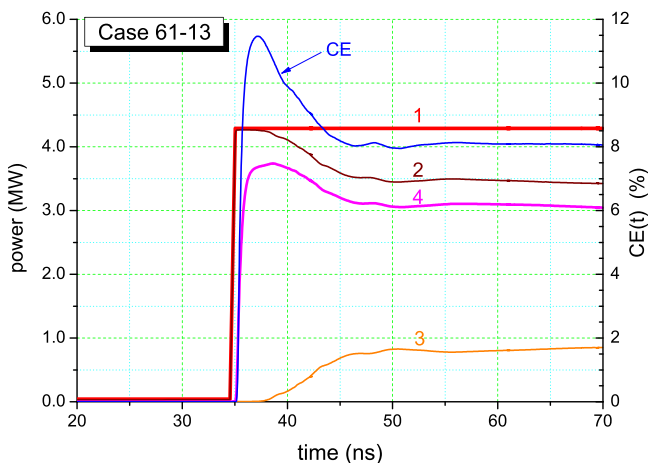


FIG. 6. Left ordinates: temporal profiles of the incident (curve 1), absorbed (curve 2), and reflected (curve 3) powers of the “master” pulse in case 61–13, as well as of the broad-band (i.e., spectrally integrated) EUV power (curve 4). Right ordinates: temporal profile of the instantaneous conversion efficiency $CE(t)$.

reabsorption of the in-band EUV flux in the expanding plasma. The relative role of factor (i) can be evaluated by noticing that at $t = 37.2$ ns about 86% of the absorbed laser power is converted into the broad-band EUV (see Fig. 6). When corrected for this factor, the peak CE would amount to $\approx 13.4\%$ —still well below the expected 20%. The latter implies that factors (ii) and (iii) make a decisive contribution to degradation of the peak SP, with their individual inputs being, however, difficult to separate.

The passive-phase density profile, established by $t = 35$ ns, represents a steady ablation flow induced by the “slave” laser alone. Once the “master” laser is turned on, there begins a transition to a new steady-state configuration, controlled primarily by the “master” pulse and characterized by a new *active-phase* density profile. This transition involves two different timescales, namely, a relatively quick (within 1–2 ns) rise of the plasma temperature, followed by a somewhat slower (within 5–10 ns) reshaping (steepening) of its spatial density profile as is shown in Fig. 7. The corresponding evolution of the 2D density distribution is displayed in Fig. 8. As a result, we observe a transient peak $CE(t) = CE_{tp}$ of the conversion efficiency, produced by a brief beneficial combination of the optimal plasma temperature with the shallow passive-phase density gradient. Later on, as the n_e profile steepens and approaches its active-phase equilibrium, the conversion efficiency $CE(t)$ decreases and settles to its final steady-state value of $CE(t) = CE_{st} < CE_{tp}$.

The decrease of $CE(t)$ from its peak value $CE_{tp} = 11.5\%$ to the steady-state level of $CE_{st} \approx 8.1\%$ is caused by two main factors, namely, (i) by the enhanced laser reflection from a steepened n_e profile and (ii) by the increased degree of temperature and ionization non-uniformity across the laser absorbing volume. Because at $t > 47$ ns the laser reflection rises to 17%–18%, the factor (i) alone accounts for a $CE(t)$ reduction from 11.5% to about 9.5%. Further reduction down to 8.1% is caused by an increased span of temperature variation across the laser absorption zone, as is illustrated in Fig. 9. Remarkably, the ratio of the total (broad-band) EUV

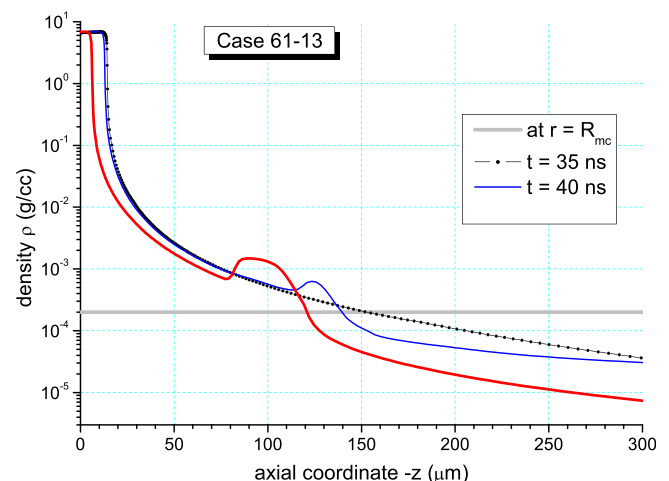


FIG. 7. Plasma density profiles in case 61–13 along the laser axis at different times once the “master” laser has been turned on at $t = 35$ ns. The thick horizontal line represents the density at the critical surface $r = R_{mc}$ of the “master” laser.

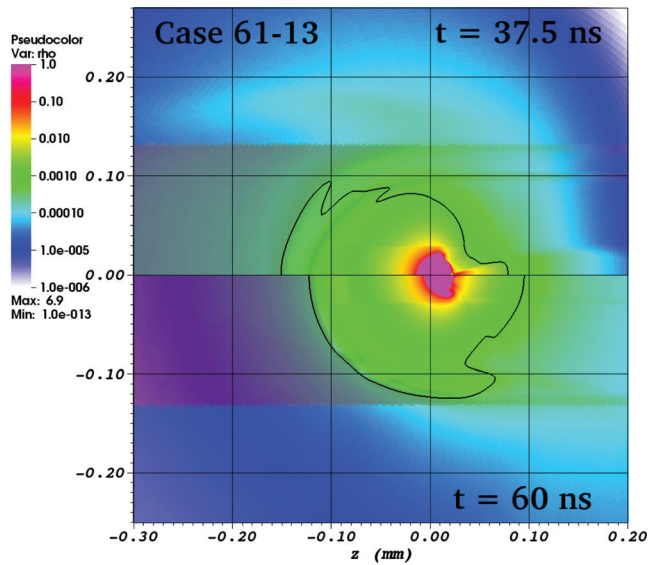


FIG. 8. 2D plasma density (in g/cc) map in case 61-13 at $t = 37.5$ ns and 60 ns. The black contour marks the critical surface $n_e = 10^{19} \text{ cm}^{-3}$ for the CO_2 laser. The intensity of the two illuminating lasers is represented by dark shadows.

emission power to the absorbed laser power remains quite stable throughout this stage at about 90%. The latter means that, beside the decreasing laser absorption, it is the degradation of the spectral purity rather than the higher conversion into the plasma kinetic energy, which mainly contributes to the fall of $\text{CE}(t)$.

B. Results of optimization

The above discussion implies that, when optimizing for maximum CE, one can aim either at a maximum peak value CE_{tp} , or at a maximum steady-state value CE_{st} , or at a maximum time-integrated value (for which we preserve the regular notation CE). Evidently, the optimization procedure, outlined in Sec. V, applies to the transient peak CE_{tp} because it relies on the passive-phase density profile prepared by the “slave” laser. In what concerns the maxima of CE and CE_{st} , affected by the transition to the active-phase profiles, the optimization strategy and its parametrization still remain as described in Sec. V, although the corresponding maxima may occur at different values of I_{ml} and R_{mc} .

Here, we present the results obtained by running several 1D optimizations with respect to the “master” intensity I_{ml} for different values of the flow scale R_{mc} , controlled by the droplet radius R_d and the “slave” laser wavelength λ_{sl} as given by Eq. (12). The intensity of the “slave” laser was fixed at $I_{sl} = 1.5 \times 10^9 \text{ W/cm}^2$ on a spot with radius $r_{sl,foc} = 1.5R_d$. The focal radius $r_{ml,foc}$ of the “master” pulse was chosen somewhat below R_{mc} , so that no laser light missed the target unabsorbed (or unreflected). Every individual simulation was terminated after 35 ns of operation of the “master” laser.

Figure 10 shows the results of the 1D optimization with respect to I_{ml} for the case of $R_d = 20 \mu\text{m}$, for which the absolute maximum of $\text{CE}_{tp} = 11.5\%$ was found. In full agreement with the arguments of Sec. V, the plots of CE and CE_{tp} versus

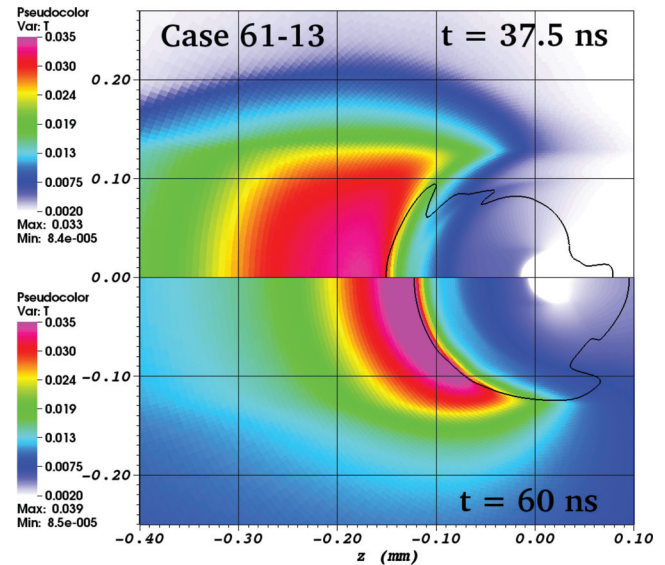


FIG. 9. Same as Fig. 8 but for the plasma temperature (in keV). Recall that efficient EUV emission at 13.5 nm comes from the region with $25 \text{ eV} \approx T \approx 35 \text{ eV}$.

I_{ml} exhibit though flat but distinct maxima, namely, at $I_{ml} \approx 7 \times 10^9 \text{ W/cm}^2$ for the time-integrated CE, and at $I_{ml} \approx 9 \times 10^9 \text{ W/cm}^2$ for the transient peak CE_{tp} . As expected, the back reflection of the laser light grows monotonically with I_{ml} because, on the one hand, the final equilibrium n_e profile near the critical surface becomes steeper, and, on the other hand, the electron temperature at the critical surface increases, causing the electron-ion collision frequency to drop.

Table I presents the main optimization results with respect to both relevant parameters I_{ml} and R_{mc} . For each value of R_{mc} , the maximum values of CE_{tp} , CE_{st} , and CE, obtained through the 1D optimization with respect to I_{ml} , are given. The time-integrated laser absorption fraction $f_{a,ml}$ corresponds to the maximum of the integral conversion efficiency CE.

From Table I, one learns that the absolute maximum of the transient peak CE_{tp} is achieved for the source size $R_{mc} \simeq 150 \mu\text{m}$. At the same time, the local (with respect to I_{ml} only) maxima of the steady-state CE_{st} and of the integral CE continue to grow—although slowly—even beyond the source

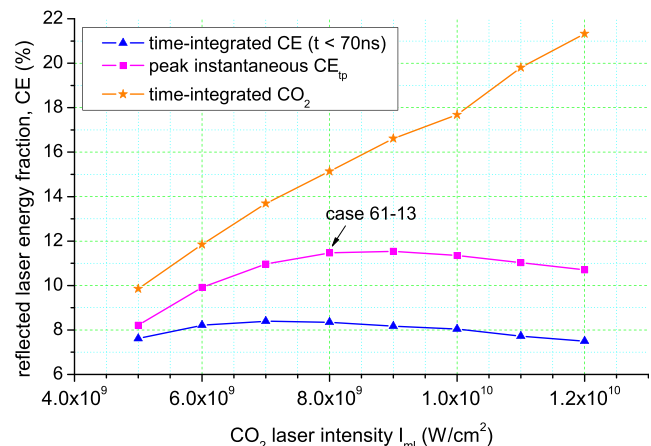


FIG. 10. Results of the one-dimensional optimization with respect to the “master” laser intensity I_{ml} for a tin droplet with radius $R_d = 20 \mu\text{m}$.

radius $R_{mc} = 300 \mu\text{m}$. To explain this behavior, one has to recall that the main cause for degradation of CE for too large values of R_{mc} is the increasing self-absorption of the in-band emission as the density gradient flattens. For one and the same R_{mc} , the length scale near the critical surface (hence the optical thickness τ_{uv} for the in-band EUV) along the steepened active-phase profile (the $t = 60 \text{ ns}$ curve in Fig. 7) is significantly shorter than that along the shallow passive-phase profile (the $t = 35 \text{ ns}$ curve). As a result, the saturation of the maximum steady-state conversion efficiency CE_{st} with the increasing R_{mc} due to the growing self-absorption occurs significantly later than the corresponding saturation of CE_{tp} , namely, at source radii $R_{mc} > 300 \mu\text{m}$ not pursued in this study. The evident leveling-off of the steady-state CE_{st} at source diameters $2R_{mc} \approx 400 \mu\text{m}$ agrees with the earlier observations of the same effect for the Nd:YAG laser.³²

VII. SOLUTION WITHOUT THE “SLAVE” LASER

The principal function of the “slave” laser in our scheme is to provide an independent (of the “master” laser and of the droplet size) control over the mass ablation rate and, eventually, over the spatial scale across the absorption region for the main pulse. If the “slave” laser is removed, a steady “master” pulse alone produces finally a configuration with a certain steady (for a given droplet radius R_d) ablation rate, which corresponds to a certain quasi-stationary source radius R_{mc} . We assume that the irradiation intensity I_{ml} is at its optimum value, dictated by the optimum temperature in the working zone. Of course, a steady ablation flow establishes itself after a certain relaxation period, as the critical surface of the “master” pulse gradually swells around the ablated droplet to its quasi-stationary position.

Relaxation to a steady state under the “master” pulse alone is illustrated in Figs. 11 and 12, where the simulation

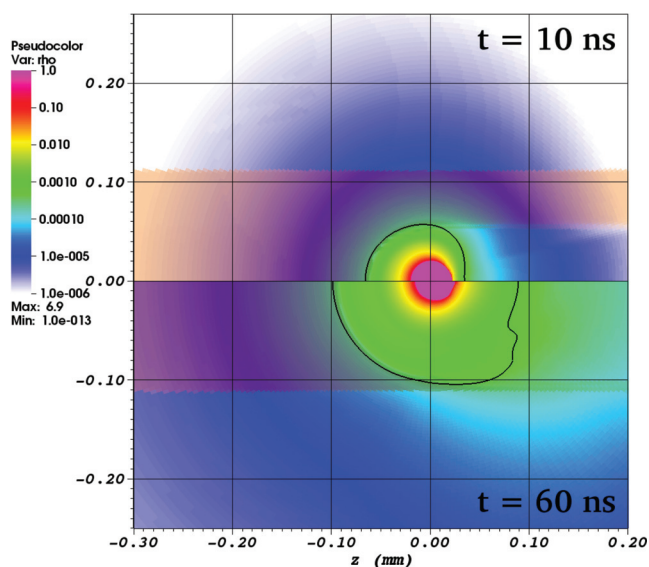


FIG. 11. Plasma density map around a $40\text{-}\mu\text{m}$ diameter droplet, irradiated by the CO_2 laser alone with the intensity $I_{ml} = 8 \times 10^9 \text{ W/cm}^2$, at two different times $t = 10 \text{ ns}$ (upper half) and $t = 60 \text{ ns}$ (lower half). The black contour marks the position of the critical surface at $n_e = 10^{19} \text{ cm}^{-3}$. The local laser intensity is indicated as a brown shadow.

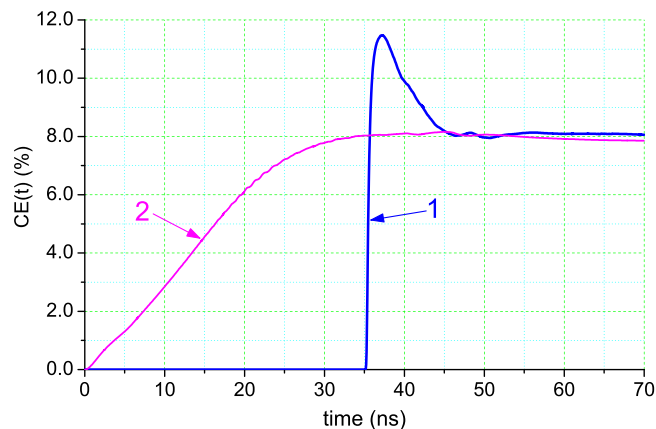


FIG. 12. Instantaneous conversion efficiency as a function of time for the cases with (curve 1) and without (curve 2) the “slave” laser. In both cases the intensity of the CO_2 “master” laser was $I_{ml} = 8 \times 10^9 \text{ W/cm}^2$.

results for a $R_d = 20 \mu\text{m}$ droplet, irradiated by a CO_2 laser pulse with a fixed intensity of $I_{ml} = 8 \times 10^9 \text{ W/cm}^2$, are shown. The only difference with the earlier discussed case 61–13 is the absence of the “slave” pulse and a somewhat smaller ($r_{foc,ml} = 110 \mu\text{m}$ instead of $r_{foc,ml} = 130 \mu\text{m}$) focal spot of the CO_2 pulse. One sees that the reduction of R_{mc} , caused by the removal of the “slave” pulse with $\lambda_{sl} = 0.352 \mu\text{m}$, is by no means dramatic. Note that, without the “slave” pulse, optimization of CE with respect to the plasma length scale R_{mc} can only be done by varying the droplet radius R_d (or using a different target geometry—an option not considered here).

Figure 12 compares the temporal profile of the instantaneous $CE(t)$, calculated without the “slave” pulse (curve 2), with that from case 61–13 (curve 1). At $t > 30 \text{ ns}$, after the ablation flow relaxes to its steady-state configuration, curve 2 stabilizes at practically the same value as the asymptotic level of curve 1. In other words, the steady-state conversion efficiency CE_{st} is practically independent of the presence of the “slave” laser, provided that the entire laser beam is intercepted by the ablated plasma cloud. On the other hand, high energy cost of attaining the steady-state configuration under the “master” pulse noticeably degrades the integral CE (from 8.3% to 6.4% for the cases shown in Fig. 12), especially when the total pulse duration is below 100 ns.

VIII. CONCLUSION

Under the conditions of steady-state ablation of the Sn plasma, the conversion efficiency of the laser energy into the 13.5-nm EUV emission is mainly controlled by two factors, namely, (i) by the intensity I_{ml} of the main (“master”) laser pulse and (ii) by the spatial structure of the flow region in the absorption zone of the main pulse. Two different-color lasers provide a means of independent control over these two factors, and a possibility to perform a full optimization study in quest for maximum CE.

Under realistic conditions, the flow geometry must, on the one hand, be open from at least one side to ensure the delivery of the main pulse to the working zone, and, on the

other hand, be as uniform as possible across this zone. A reasonable compromise appears to be a steady quasi-spherically diverging flow, where the length scale of variation of all plasma parameters is simply the radius R_{mc} of the laser absorption region. Because the laser irradiates the target from only one side, the problem becomes essentially two- or three-dimensional.

In this work, the detailed arguments are presented why CE must have an absolute maximum with respect to the two essential parameters I_{ml} and R_{mc} , and the optimization strategy for calculating this maximum is described. For the main pulse, provided by a CO₂ laser with $\lambda = 10.6 \mu\text{m}$, this maximum was found by performing an optimization study with the 2D RHD code RALEF. Within the physics model implemented in RALEF, the sought-for maximum turns out to be $\text{CE}_{ip} \approx 11.5\%$. This optimum occurs at $I_{ml} \approx 8 \times 10^9 \text{ W/cm}^2$ and $R_{mc} \approx 150 \mu\text{m}$, but is of transient nature and represents the instantaneous CE value during a short period of 1–2 ns.

In comparison, the CE maximum of the relaxed steady-state configuration was found to be more modest, $\text{CE}_{st} \approx 9\%$, and to occur at a considerably larger flow scale $R_{mc} \approx 300 \mu\text{m}$. The latter is explained by the fact that, under steady irradiation by the “master” pulse, the spatial structure of the laser absorption zone changes to a less homogeneous—i.e., less efficient—configuration than the one produced by the “slave” laser alone. Another implication of this fact is that the ability of the “slave” laser to provide an independent control over the uniformity of the main-pulse absorption zone is rather limited.

As a word of caution, it should be emphasized that the atomic-physics and level-kinetics models, on which the radiation transport in the present simulations was based, rely on several major simplifications, like a steady-state CR approximation and partially opaque k_ν tables (see Sec. III for details). In addition, all the effects contributing to eventual transverse plasma non-uniformities, like laser refraction and/or non-uniform focal spots, have been deliberately ignored. Once these simplifications are removed (or refined), the specific values of the maximum CE and the optimum I_{ml} and R_{mc} values, calculated in this work, may change. Any additional plasma non-uniformities across the working zone generally tend to degrade the maximum CE. On the other hand, retardation in reaching the ionization equilibrium and departures from the partially opaque approximation by calculating the plasma spectral emissivity is expected to generally enhance the optimum CE values. Despite such uncertainties, the present study should adequately reproduce the principal interrelations and the relative contributions of the key physical effects determining the maximum possible CE values for the purposes of the EUV lithography.

ACKNOWLEDGMENTS

This work was supported by the Russian Science Foundation through Grant No. 14-11-00699. The author is grateful to A. Bratchenia and K. Tsigutkin for pointing out potential advantages of combining two different-color lasers.

The reported extensive 2D simulations have been carried out on the K-100 supercomputer at the Keldysh Institute of Applied Mathematics in Moscow.

- ¹V. Bakshi, *EUV Sources for Lithography*, Press Monographs (SPIE Press, 2006).
- ²V. Y. Banine, K. N. Koshelev, and G. H. P. M. Swinkels, *J. Phys. D: Appl. Phys.* **44**, 253001 (2011).
- ³T. Aota and T. Tomie, *Phys. Rev. Lett.* **94**, 015004 (2005).
- ⁴A. Cummings, G. O’Sullivan, P. Dunne, E. Sokell, N. Murphy, and J. White, *J. Phys. D: Appl. Phys.* **38**, 604 (2005).
- ⁵M. Murakami, S. Fujioka, H. Nishimura, T. Ando, N. Ueda, Y. Shimada, and M. Yamaura, *Phys. Plasmas* **13**, 033107 (2006).
- ⁶K. Nishihara, A. Sasaki, A. Sunahara, and T. Nishikawa, in *EUV Sources for Lithography*, edited by V. Bakshi (SPIE Press, Bellingham, Washington, USA, 2006), pp. 339–370.
- ⁷K. Nishihara, A. Sunahara, A. Sasaki, M. Nunami, H. Tanuma, S. Fujioka, Y. Shimada, K. Fujima, H. Furukawa, T. Kato, F. Koike, R. More, M. Murakami, T. Nishikawa, V. Zhakhovskii, K. Gamata, A. Takata, H. Ueda, H. Nishimura, Y. Izawa, N. Miyanaga, and K. Mima, *Phys. Plasmas* **15**, 056708 (2008).
- ⁸K. Nishihara, A. Sunahara, A. Sasaki, S. Fujioka, Y. Shimada, M. Nunami, H. Tanuma, M. Murakami, T. Aota, K. Fujima, H. Furukawa, T. Nishikawa, F. Koike, R. More, T. Kato, V. Zhakhovskii, K. Gamata, H. Ueda, H. Nishimura, Y. Yuba, K. Nagai, N. Miyanaga, Y. Izawa, and K. Mima, *Proc. SPIE* **6921**, 69210Y (2008).
- ⁹Y. Tao, M. S. Tillack, K. L. Sequoia, R. A. Burdt, S. Yuspeh, and F. Najmabadi, *Appl. Phys. Lett.* **92**, 251501 (2008).
- ¹⁰A. Hassanein, T. Sizyuk, V. Sizyuk, and S. S. Harilal, *J. Micro/Nanolithography, MEMS MOEMS* **10**, 033002 (2011).
- ¹¹S. Fujioka, M. Shimomura, Y. Shimada, S. Maeda, H. Sakaguchi, Y. Nakai, T. Aota, H. Nishimura, N. Ozaki, A. Sunahara, K. Nishihara, N. Miyanaga, Y. Izawa, and K. Mima, *Appl. Phys. Lett.* **92**, 241502 (2008).
- ¹²J. R. Freeman, S. S. Harilal, and A. Hassanein, *J. Appl. Phys.* **110**, 083303 (2011).
- ¹³A. F. Nikiforov, V. G. Novikov, and V. B. Uvarov, *Quantum-Statistical Models of Hot Dense Matter: Methods for Computation Opacity and Equation of State (Progress in Mathematical Physics)*, 1st ed. (Birkhäuser, Basel, 2005).
- ¹⁴J. Bauche, C. Bauche-Arnoult, and O. Peyrusse, *Atomic Properties in Hot Plasmas: From Levels to Superconfigurations* (Springer International Publishing, 2015).
- ¹⁵V. G. Novikov, V. V. Ivanov, K. N. Koshelev, V. M. Krivtsov, and A. D. Solomyannaya, *High Energy Density Phys.* **3**, 198 (2007).
- ¹⁶I. Tolstikhina, S. Churilov, A. Ryabtsev, and K. Koshelev, in *EUV Sources for Lithography*, edited by V. Bakshi (SPIE Press, Bellingham, Washington, USA, 2006), pp. 113–148.
- ¹⁷M. M. Basko, J. A. Maruhn, and A. Tauschwitz, “Development of a 2D radiation-hydrodynamics code RALEF for laser plasma simulations,” GSI Report 2010-1, PLASMA-PHYSICS-25 (GSI Helmholtzzentrum für Schwerionenforschung GmbH, 2010).
- ¹⁸M. M. Basko, P. V. Sasorov, M. Murakami, V. G. Novikov, and A. S. Grushin, *Plasma Phys. Controlled Fusion* **54**, 055003 (2012).
- ¹⁹F. L. Addessio, J. R. Baumgardner, J. K. Dukowicz, N. L. Johnson, B. A. Kashiwa, R. M. Rauenzahn, and C. Zemach, “CAVEAT: A computer code for fluid dynamics problems with large distortion and internal slip,” Report No. LA-10613-MS-Rev. 1, UC-32 (Los Alamos National Laboratory, 1992).
- ²⁰E. Livne and A. Glasner, *J. Comput. Phys.* **58**, 59 (1985).
- ²¹M. M. Basko, J. A. Maruhn, and A. Tauschwitz, *J. Comput. Phys.* **228**, 2175 (2009).
- ²²A. Dedner and P. Vollmöller, *J. Comput. Phys.* **178**, 263 (2002).
- ²³E. W. Larsen, J. E. Morel, and W. F. Miller, Jr., *J. Comput. Phys.* **69**, 283 (1987).
- ²⁴S. Faik, M. M. Basko, A. Tauschwitz, I. Iosilevskiy, and J. A. Maruhn, *High Energy Density Phys.* **8**, 349 (2012).
- ²⁵M. M. Basko, T. Löwer, V. N. Kondrashov, A. Kendl, R. Sigel, and J. Meyer-ter Vehn, *Phys. Rev. E* **56**, 1019 (1997).
- ²⁶M. Born, E. Wolf, A. Bhatia, P. Clemmow, D. Gabor, A. Stokes, A. Taylor, P. Wayman, and W. Wilcock, *Principles of Optics: Electromagnetic Theory of Propagation, Interference and Diffraction of Light* (Cambridge University Press, 1999).

- ²⁷W. Kruer, *The Physics of Laser Plasma Interactions*, Frontiers in Physics (Addison-Wesley, 1988).
- ²⁸P. Mora, *Phys. Fluids* **25**, 1051 (1982).
- ²⁹M. M. Basko, V. G. Novikov, and A. S. Grushin, *Phys. Plasmas* **22**, 053111 (2015).
- ³⁰L. Oster, *Rev. Mod. Phys.* **33**, 525 (1961).
- ³¹A. Sasaki, A. Sunahara, H. Furukawa, K. Nishihara, S. Fujioka, T. Nishikawa, F. Koike, H. Ohashi, and H. Tanuma, *J. Appl. Phys.* **107**, 113303 (2010).
- ³²R. C. Spitzer, T. J. Orzechowski, D. W. Phillion, R. L. Kauffman, and C. Cerjan, *J. Appl. Phys.* **79**, 2251 (1996).